RSC Advances

ROYAL SOCIETY OF CHEMISTRY

PAPER

View Article Online
View Journal | View Issue

Check for updates

Cite this: *RSC Adv.*, 2025, **15**, 43275

Biowaste-derived porous nano-carbon-supported transition metal borides as efficient electrocatalysts for alkaline water splitting: a waste-to-wealth approach

B. Sirichandana,[ab] R. Silviya,[c] Uraiwan Sirimahachai,[d] Nainesh Patel[c] and Gurumurthy Hegde*[ae]

Received 12th August 2025
Accepted 20th October 2025

DOI: 10.1039/d5ra05923b

rsc.li/rsc-advances

The development of high-performance and cost-effective electrocatalysts for water splitting is crucial for addressing the growing global energy demand and mitigating future energy crisis. In this study, a simple two-step strategy involving pyrolysis and chemical reduction was employed to synthesize a biomass-derived carbon-based electrocatalyst. Biowaste onion peel-based precursors synthesized at 1000 °C *via* pyrolysis showed the best performance as a support for transition metal borides in comparison with the same synthesized at temperatures of 600 and 800 °C. Furthermore, a series of carbon-supported metal boride catalysts, ON10/Co–B, ON10/Ni–B, and ON10/Fe–B, were synthesized and systematically tested for their electrochemical performance towards alkaline water splitting. Among the synthesized electrocatalysts, ON10/Co–B showed the best electrocatalytic activity with an overpotential of −122 mV for the HER at a current density of 10 mA cm^{-2}. The catalyst ON10/Co–B also exhibited excellent stability for over 40 h and a durability for ∼1000 cycles in alkaline conditions. The enhanced electrocatalytic activity of ON10/Co–B for the HER is the result of the combined effect of the carbon support and Co–B. This work demonstrates the potential of biomass-derived carbon-supported transition metal borides as efficient and sustainable electrocatalysts for the HER.

1. Introduction

Hydrogen (H_2) is considered a clean energy carrier, offering a promising alternative to fossil fuels for meeting future energy demands with net zero emissions.[1] Among the various methods of hydrogen production, electrochemical water splitting is an efficient technique for the production of high-purity hydrogen using renewable energy.[2] The major challenges include the design and development of low-cost and high-performance electrocatalysts to overcome the kinetic barriers of two half reactions, namely, the HER at the cathode and the OER at the anode, during water splitting. Pt is considered the state-of-the-art catalyst for the HER, and RuO_2 and IrO_2 are effective catalysts used for the OER.[3] However, the high cost and limited abundance of these noble metals make the process economically unviable for large-scale applications. In order to address this, alternative non-noble metals with similar efficiencies have been explored.[4]

In the past decade, various forms of transition metals, including oxides,[5] borides,[6] selenides,[7] sulphides,[8] and phosphides,[9] have been reported as electrocatalysts for water splitting. Particularly, transition metal borides are studied for electrochemical applications, whose combination of metal and boron at the nanoscale imparts them with unique structural and electrical properties.[10] The amorphous nature of transition metal borides creates a large number of active sites, which are beneficial for enhancing the electrocatalytic activity towards the HER.[10,11] Apart from these, the reverse electron transfer mechanism exhibited by amorphous transition metal borides, where electrons are donated to metal sites by boron, aids in maintaining an optimal electron density on metal sites and helps to prevent the oxidation of active metal sites, making them suitable electrocatalysts for water splitting.[12] Despite their promising traits, the industrial viability of borides is limited by particle agglomeration, which can be addressed by decorating the boride particles on the porous and conducting support.

Carbon-based nanomaterials are increasingly recognized as vital electrocatalyst supports for electrolysis owing to their superior electrical conductivity, porous architecture, high

---

[a] *Department of Chemistry, Christ University, Hosur Road, Bengaluru 560029, India*

[b] *Centre for Renewable Energy and Environmental Sustainability, Christ University, Bangalore, Karnataka 560029, India*

[c] *Department of Physics and Electronics, Christ University, Hosur Road, Bengaluru 560029, India*

[d] *Centre of Excellence for Innovation in Chemistry, Division of Physical Science, Faculty of Science, Prince of Songkla University, Hat Yai, Songkla 90112, Thailand*

[e] *Centre for Advanced Research and Development (CARD), Christ University, Hosur Road, Bengaluru 560029, India. E-mail: murthyhegde@gmail.com*

surface area, physicochemical stability, and enhanced dispersion of active sites. Various forms of carbon nanomaterials such as graphenes, carbon nanotubes, reduced graphene oxide, and carbon nanosheets combined with transition metal oxides, phosphides, dichalcogenides and carbides have been studied for the HER, where the combined effect of carbon and metal forms have been proven with the increased electrochemical performance through the formation of more exposed active sites and efficient electron transfer.[13–15] Generally, carbon nanomaterials are synthesized using fossil fuel-based precursors, involving energy-demanding processes such as laser ablation, chemical vapour deposition, and electric arc discharge, and also include the use of toxic chemicals, which make the synthesis of carbon expensive and environmentally harmful.[16] Biomass-derived carbon uses sustainable, low-cost precursors for the synthesis of carbon with tailored porosity, morphology, size, and stability, highlighting a waste-to-wealth approach.

India, one of the largest exporters of onions, not only produces large amounts of waste onion peels but also causes environmental pollution if not tackled in an effective manner. In this work, we used such onion peels to produce carbon nanospheres (CNSs) by a simple and effective pyrolysis technique.[17] CNSs are a type of carbon material in which graphite sheets appear as wavy flakes that form spherical structures with exposed edges, which are considered to be active and aid in electrochemical performance.[18] CNSs were synthesized from onion peels at three different temperatures, namely, 600 °C, 800 °C, and 1000 °C without the addition of any activating agents. Subsequently, the synthesized CNSs were integrated with transition metal borides (Co–B, Ni–B, and Fe–B) by a simple chemical reduction method. The main objective of the work is to study the effect of synthesis temperature on the properties of carbon and the subsequent effect on the electrochemical performance of alkaline water splitting. The series of catalysts were electrochemically tested and characterized by physicochemical techniques. Among the catalysts tested, ON10/Co–B exhibited the best electrocatalytic performance for the HER. The robustness of the optimized electrocatalyst was tested through stability and durability tests. This study provides insights into how synthesis conditions influence catalytic activity and also presents that carbon materials obtained from the biomass can effectively function as sustainable and low-cost electrocatalysts for the alkaline water splitting.

2. Experimental

2.1. Synthesis of carbon nanospheres

Onion peels were chosen as raw precursor for the synthesis of CNSs. The collected onion peels were dried, finely powdered, and sieved using a 75 μm sieve. The sieved precursor was subjected to pyrolysis at 600 °C, 800 °C, and 1000 °C with continuous nitrogen flow. The obtained CNSs were washed with 0.1 M HCl and subsequently with distilled water and ethanol. The CNSs synthesized at 600 °C, 800 °C, and 1000 °C were labelled as ON6, ON8, and ON10, respectively. A detailed synthesis procedure can be found in our earlier work.[17]

2.2. Synthesis of the catalyst

Carbon-supported metal borides were prepared by the chemical reduction method. In a beaker containing 20 ml of water, $CoCl_2 \cdot 6H_2O$ was added first and then the synthesized CNSs were added, and sonicated for 20 minutes. To this suspension, $NaBH_4$ (five times the molar ratio of Co) was added in order to ensure complete reduction of metal ions under stirring conditions. $NaBH_4$ serves both as a boron source and a strong reducing agent. The obtained black precipitate was collected after 15 minutes of stirring and washed thoroughly with water and ethanol. For the optimization studies, CNSs and $CoCl_2 \cdot 6H_2O$ were used in different weight ratios of 1 : 1, 2 : 1, and 3 : 1 referred to as the carbon-to-metal (C : M) ratio. The same procedure was followed by using the CNSs synthesized at 600 °C, 800 °C, and 1000 °C and labelled as ON6/Co–B, ON8/Co–B, and ON10/Co–B, respectively. Similarly, ON10/Ni–B and ON10/Fe–B were synthesized using ON10 with nickel chloride hexahydrate and ferric chloride anhydrous, respectively.

3. Results and discussion

Onion peels with ~38% lignin, ~16% hemicellulose, and ~40% cellulose were chosen as the precursor for the synthesis of carbon nanospheres.[19] The onion peels were subjected to pyrolysis at 600 °C, 800 °C, and 1000 °C without using any activating agents, resulting in ON6, ON8, and ON10, respectively. Further, the carbon-supported transition metal borides (ON/Co–B, ON/Ni–B, and ON/Fe–B) were synthesized by the chemical reduction method. The detailed synthesis procedure is shown in Fig. 1. The TGA curve of the biomass precursor ON-raw, as shown in Fig. S1a, illustrates its thermal decomposition pattern. An initial weight loss of 11.76% occurred near 200 °C, which is mainly attributed to the loss of moisture from the ON-raw sample. A major weight loss of 51.44% was recorded between 200 °C and 400 °C, which is associated with the thermal breakdown of cellulose, hemicellulose, and lignin components in the precursor. After 400 °C, only a slight mass loss was noted, which can be attributed to the slow pyrolysis of lignin.[20] These results support the selection of 600 °C, 800 °C, and 1000 °C as the pyrolysis temperatures for CNSs preparation. The TGA plots of ON6, ON8, and ON10 are given in Fig. S1b. As can be seen from the plot, ON10 shows excellent thermal stability, exhibiting no notable weight loss except below 100 °C, which is probably due to the release of moisture.

The FTIR analysis (Fig. 2a) of raw precursor (ON-raw) showed a broad peak near 3400 cm^{-1}, attributed to the O–H stretching vibrations of the cellulosic structures and water molecules; a peak at 2915 cm^{-1} corresponded to C–H bond stretching in lignocellulosic components of onion peel. The intense band at nearly 1030 cm^{-1} can be due to the C–O–C glycosidic linkage of hemicellulose and cellulose moieties.[21] The peaks that appeared at 1600 cm^{-1} could be due to the C═O stretching vibrations. These results indicate that the precursor predominantly contains cellulose, hemicellulose, and lignocellulose, making it a viable carbon source for carbon nanosphere synthesis. In the FTIR spectrum of ON10 (Fig. 2a), the disappearance of the

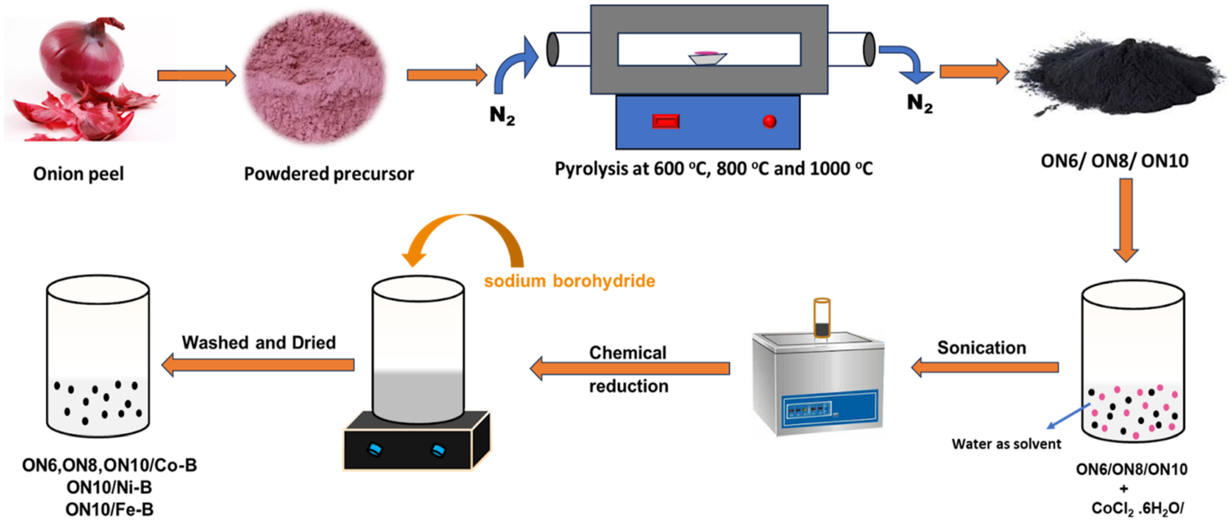

Fig. 1 Schematic of the synthesis of carbon and carbon-supported transition metal borides.

C–O–C glycosidic linkage peak confirms the complete breakdown of lignocellulosic structures and the removal of volatile compounds during high-temperature treatment, leading to the formation of carbon nanoparticles with a higher carbon content and a lower oxygen content.

In order to study the effect of synthesis temperature on the formation of carbon nanospheres, ON6, ON8, and ON10 were analyzed by characterization techniques such as XRD, Raman spectroscopy, FESEM, EDS, and BET. The XRD patterns for all the prepared carbon nanostructures, ON6, ON8, and ON10 are depicted in Fig. 2b. The XRD peaks observed at $2\theta \approx 24°$ and $2\theta \approx 44°$ were ascribed to the (002) and (100) planes of graphitized carbon, respectively.[22] The not-so-well defined XRD pattern at the (100) plane in ON6 hinted at the ongoing structural transformations. At higher temperatures, the appearance of broader peaks corresponding to the (002) and (100) planes of graphitic carbon was observed.

The structural properties of the synthesized carbon were studied from Raman analysis. The Raman spectra of ON6, ON8, and ON10 are given in Fig. 2c. Two prominent peaks at nearly 1350 cm^{-1} and 1590 cm^{-1} were observed in all the synthesized carbon. The peak at 1350 cm^{-1} corresponds to the D band, and the peak at 1590 cm^{-1} corresponds to the G band in the carbon lattice. The D-band indicates disordered graphite, and the G-band is due to the E_{2g} vibration of sp^2-bonded carbons in a graphitic lattice.[23] With the increase in carbonization temperature, an increase in I_D/I_G ratio was observed in contrast to the usual trend of getting more ordered carbons with the increased pyrolysis temperature. Similar results have been observed in earlier studies.[24] The I_D/I_G ratio was found to be 0.78, 0.97, and 0.98 for ON6, ON8, and ON10, respectively. This can be attributed to the partially disordered graphitic carbon particles. As the temperature was increased, the semi-crystalline structures were exposed to strain, which could be relieved by fracturing crystallites causing disorders.[24] The higher temperature also induces greater stress, leading to highly defective sp^2 carbon. The increasing trend of I_D/I_G values signifies the presence of a defective carbon structure, which could be beneficial for electrocatalytic performance.

To investigate the effect of synthesis temperature on the morphology and elemental composition of the synthesized carbon, the samples ON6, ON8, and ON10 were analyzed by FESEM and EDS. The formation of the carbon nanospheres started at 600 °C and exhibited nearly spherical structures, while the carbon nanoparticles synthesized at elevated temperatures of 800 °C and 1000 °C displayed a well-defined

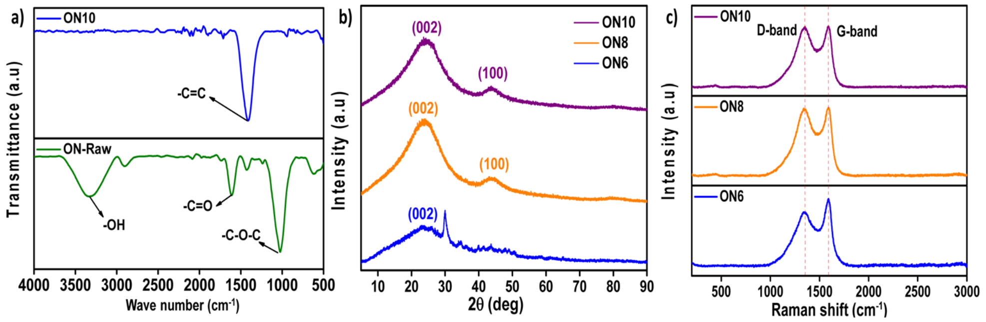

Fig. 2 (a) FTIR spectra of ON-raw and ON10. (b) XRD pattern and (c) Raman spectra of ON6, ON8, and ON10.

spherical morphology, as observed in Fig. 3a–c. It was observed that the average particle size was reduced with the increase in the synthesis temperature. When the temperature was increased from 600 °C to 1000 °C, the average size of the carbon nanospheres reduced from 90 nm to 36 nm. The decrease in particle size with the increase in pyrolysis temperature is attributed to the breakdown of solid clusters into well-defined structures. At elevated temperatures, particles undergo greater thermal stress. As they release this heat, disoriented crystallites fracture, leading to the formation of smaller particles with a spherical shape.[25] It can be observed that with the increase in synthesis temperature, the percentage of carbon content increased, as evident from the EDS analysis (Fig. S2a–c), showing that ON6, ON8, and ON10 exhibit a carbon content of 66.4%, 74% and 83.58%, respectively. ON10 showed the highest percentage of carbon content, as the majority of elements present in biomass precursors are eliminated as volatile components due to pyrolysis temperature, resulting in the formation of a carbon matrix.

The porosity of the synthesized ON6, ON8, and ON10 CNSs was studied through BET analysis, exhibiting a mean pore diameter of 3.1 nm, 2.5 nm, and 2.8 nm, respectively (Fig. S3), which is in the range of 2–50 nm, confirming the mesoporous nature of the synthesized carbon. The relative pressure (p/p_o) of ~0.94 confirms the presence of mesopores, which is advantageous to the electrochemical performance.

After careful evaluation of the physico-chemical properties of ON6, ON8, and ON10, the morphology of carbon-supported transition metal borides (ON10/Co–B, ON10/Ni–B, and ON10/Fe–B) was analyzed by FESEM. The electrochemical performance of metal borides integrated with ON10 showed the best electrocatalytic activity in comparison with ON6 and ON8, which is discussed in the later section. Hence, only the optimized catalysts ON10/Co–B, ON10/Ni–B, and ON10/Fe–B were further selected for FESEM analysis. The FESEM (Fig. 3d) and EDS (Fig. S2d) analysis of ON10/Co–B showed deposition of Co–B nanoparticles on the surface of the carbon nanospheres with elemental compositions of 55.34% of C, 19.78% of Co, 20.27% of O and 4.61% of B. Similarly, FESEM (Fig. 3e) and EDS analysis (Fig. S2e) of ON10/Ni–B showed the deposition of spherical Ni–B nanoparticles on the surface of the carbon with elemental compositions of 39.4% of C, 27.31% of O, and 20.46% of Ni, and the presence of B is observed. ON10/Fe–B showed a flake-like morphology on the surface of carbon, as shown in Fig. 3f, and the elemental percentage determined by EDS is given in Fig. S2f. The Co–B, Ni–B, and Fe–B nanoparticles were uniformly distributed across the carbon matrix, facilitated by surface dangling bonds that serve as anchoring sites. The predominant presence of oxygen can be attributed to the exposure of the

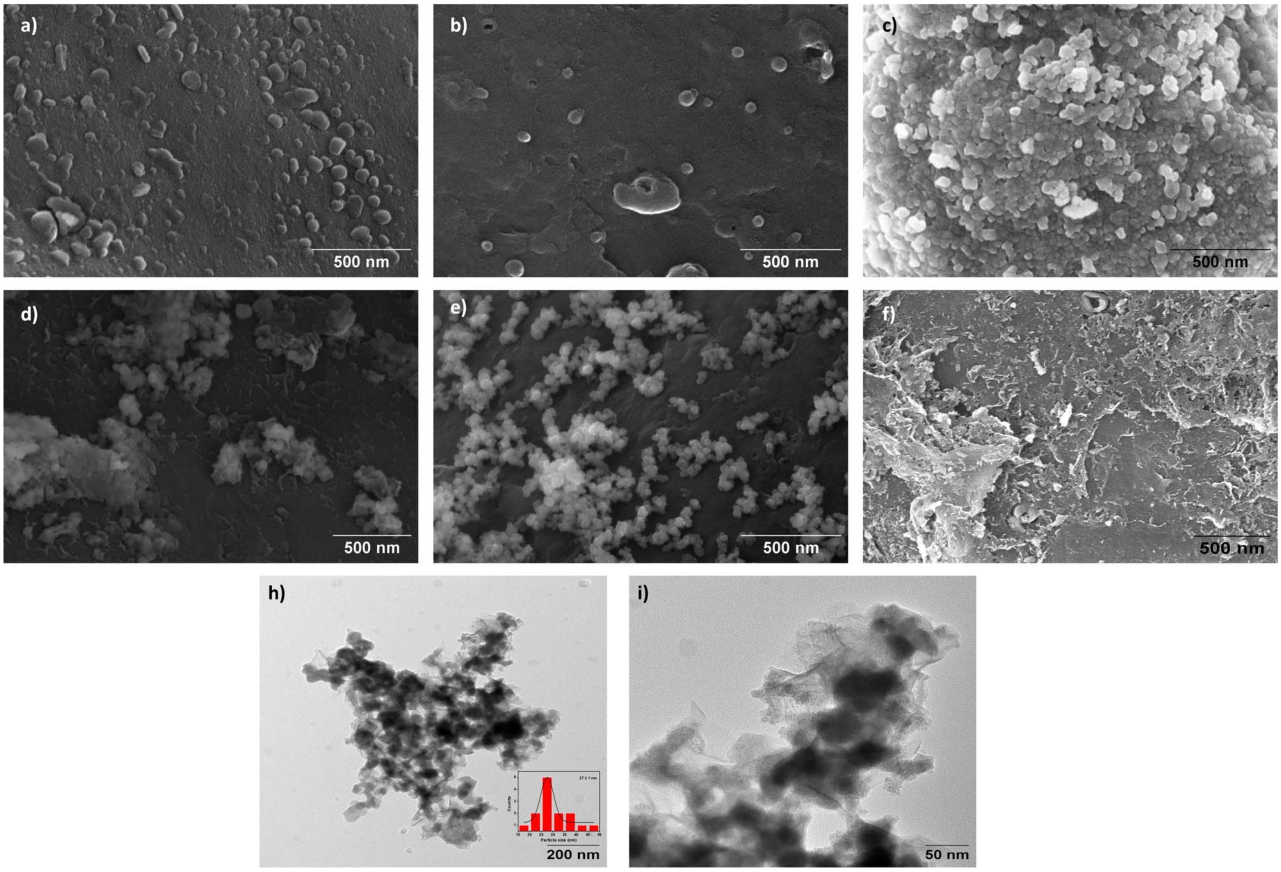

Fig. 3 FESEM images of (a) ON6, (b) ON8, (c) ON10, (d) ON10/Co–B, (e) ON10/Ni–B, and (f) ON10/Fe–B. (g) TEM image of ON10/Co–B; inset: histogram showing particle size distribution and (h) high resolution TEM image of ON10/Co–B.

electrocatalysts to atmospheric conditions; however, boron cannot be accurately detected from EDS as it is a lighter element. Upon exposure to ambient air, partial oxidation is inevitable, forming a surface layer of oxides/hydroxides.

This is a known phenomenon in metal boride systems, often resulting in a core@shell structure-metal boride core surrounded by an oxide/hydroxide shell.[26] These surface oxides/hydroxides are reduced during electrochemical activation, exposing the active metal sites during the HER. Thus, the presence of surface oxide layers does not hinder the catalytic performance. The elemental mapping (Fig. S4) of the optimized catalyst ON10/Co–B reveals a relatively homogeneous elemental distribution of Co–B on the carbon matrix. Further, the deposition of Co–B can be confirmed from the TEM image (Fig. 3g and h), where Co–B appears as dark spots on the surface of the carbon matrix with an average particle size of 27 ± 1 nm. The XRD pattern of ON10/Co–B, ON10/Ni–B, and ON10/Fe–B (Fig. S5) confirms the amorphous nature of the synthesized catalysts, which is evident from the absence of distinct diffraction peaks corresponding to a crystalline structure. The abundant undercoordinated catalytically active sites of the amorphous materials exhibit enhanced electrochemical performance in comparison with the crystalline counterparts of equivalent mass, which is advantageous for the water splitting reaction.[27] In ON10/Co–B, ON10/Ni–B, and ON10/Fe–B, the lack of distinct broad carbon peaks is ascribed to peak broadening induced by the amorphous, surface-rich Co–B, Ni–B, and Fe–B nanoparticles, rather than the loss or decomposition of carbon,[28,29] which is confirmed by XPS analysis where C 1s spectrum is evident for ON10/Co–B.

The chemical state and elemental composition of the catalysts were studied by XPS analysis. The representative survey spectrum and deconvoluted C 1s spectrum of ON10 are presented in Fig. S6d and e. The survey spectrum (Fig. S6a) of ON10/Co–B shows the peaks corresponding to C 1s, O 1s, Co 2p, and B 1s. This confirms the presence of carbon, and the deconvoluted C 1s level showed distinct peaks at 284.6 eV, 285.5 eV, 286.8 eV, 288.7 eV and 289.9 eV corresponding to C–C/C═C, C–O, C–O–C, C═O and O–C═O, respectively,[30] as given in Fig. 4a. The presence of O 1s in the catalyst, as observed in the survey spectrum, is due to the presence of carbonyl oxygen, ether, and hydroxy groups. The XPS spectrum of ON10/Co–B shows binding energies of the Co $2p_{3/2}$ and Co $2p_{1/2}$ core peaks and the corresponding satellite peaks (Fig. 4b). The binding energy (BE) peaks at 782.7 eV, 781.3 eV and 777.6 eV are assigned to Co^{2+}, Co^{3+} and elemental cobalt (Co^0), respectively.[31] In ON10/Co–B, the Co^0 peak shifts negatively by 0.5 eV relative to pure metallic cobalt (778.1 eV), indicating an electron rich state at the cobalt sites. In the B 1s spectrum (Fig. 4c), two distinct peaks appear at 187.8 eV and 191.6 eV; the first peak at 187.8 eV signifies boron–cobalt interaction,[10] whereas the second peak is attributed to oxidized boron. Compared to pure boron (187.1 eV), these peaks are shifted positively by 0.7 eV, suggesting electron transfer from boron to the vacant d-orbitals of cobalt atoms, which enhances both the catalytic activity and the structural stability. Hence, XPS analysis confirms that ON10/Co–B consists of carbon and electron-rich Co sites bonded with boron, proving the formation of carbon-supported cobalt boride. The representative XPS survey spectra of ON10/Ni–B and ON10/Fe–B are presented in Fig. S6b and S6c. The C 1s spectra (Fig. 4d and g) observed in both catalysts confirm the presence of carbon. The Ni 2p and Fe 2p spectra (Fig. 4e and h) exhibit two core-level peaks along with the characteristic satellite peaks. For ON10/Ni–B, the peak at 852.3 eV corresponds to metallic Ni^0, while the peak at 855.7 eV is attributed to Ni^{2+}.[32] In the case of ON10/Fe–B, the Fe 2p spectrum shows peaks at 707.6 eV and a peak at 711.8 eV, corresponding to metallic Fe^0 and Fe^{2+}, respectively. The peaks at 717.01 eV and 728.37 eV indicate the presence of Fe^{3+} species, arising from unavoidable surface oxidation.[33] Similar to ON10/Co–B, boron in ON10/Ni–B and ON10/Fe–B exist in both elemental and oxidized states. In ON10/Ni–B, the B 1s peaks at 191.1 eV and 187.4 eV are attributed to oxidized boron and elemental boron, respectively, as given in Fig. 4f. Similarly, elemental and oxidized boron peaks were observed in the B 1s spectrum of ON10/Fe–B (Fig. 4i). A positive shift in the binding energy of elemental boron is observed in both ON10/Ni–B and ON10/Fe–B, suggesting electron transfer from boron to metal sites.

3.1. Electrochemical studies

The electrochemical measurements of the synthesized electrocatalysts for HER were conducted in a 1 M KOH electrolyte. Based on the previous studies,[34] a carbon-to-metal ratio (C : M) of 2 : 1 was established as the optimized ratio. Accordingly, keeping the C : M ratio of 2 : 1 constant, ON6/Co–B, ON8/Co–B, and ON10/Co–B (using carbon synthesized at 600 °C, 800 °C, and 1000 °C) were synthesized, and the corresponding linear polarization curves were recorded. The cathodic LSV plot is shown in Fig. 5a. ON6/Co–B, ON8/Co–B, and ON10/Co–B display overpotentials of −230 mV, −175 mV, and −122 mV, respectively, at a benchmark current density of 10 mA cm^{-2}. These results show the improved electrocatalytic performance with the increase in pyrolysis temperature of the carbon support. An electrical equivalent circuit (see the inset in Fig. 5b) was used to analyze the impedance data, which consists of a parallel resistor–capacitor (RC). The charge transfer resistance values were found to be 4.56 Ω for ON6/Co–B, 3.96 Ω for ON8/Co–B, and 3.3 Ω for ON10/Co–B (as shown in Fig. 5b). The R_{ct} values are consistent with the HER activities of the corresponding electrocatalysts. Among the three catalysts, ON10/Co–B, in which Co–B was deposited on the carbon (ON10) synthesized at the highest pyrolysis temperature (1000 °C), exhibited the best electrocatalytic performance. This activity can be attributed to the highest carbon content, distinct spherical morphology, optimal size of the nanoparticle, porosity, and disordered nature of ON10 (confirmed by characterization techniques), which helps in the generation of more active sites by improved dispersion of Co–B on the surface of ON10. Hence, ON10 was taken for further studies. To confirm the influence of the C : M ratio, ON10/Co–B was prepared with ratios of 1 : 1, 2 : 1, and 3 : 1. The corresponding overpotentials at a current density of 10 mA cm^{-2} were −161 mV, −122 mV, and −239 mV, while the R_{ct} values were 3.65 Ω, 3.31 Ω, and 4.56 Ω, respectively (Fig. 5c). Based on these results, the 2 : 1 C : M ratio exhibited

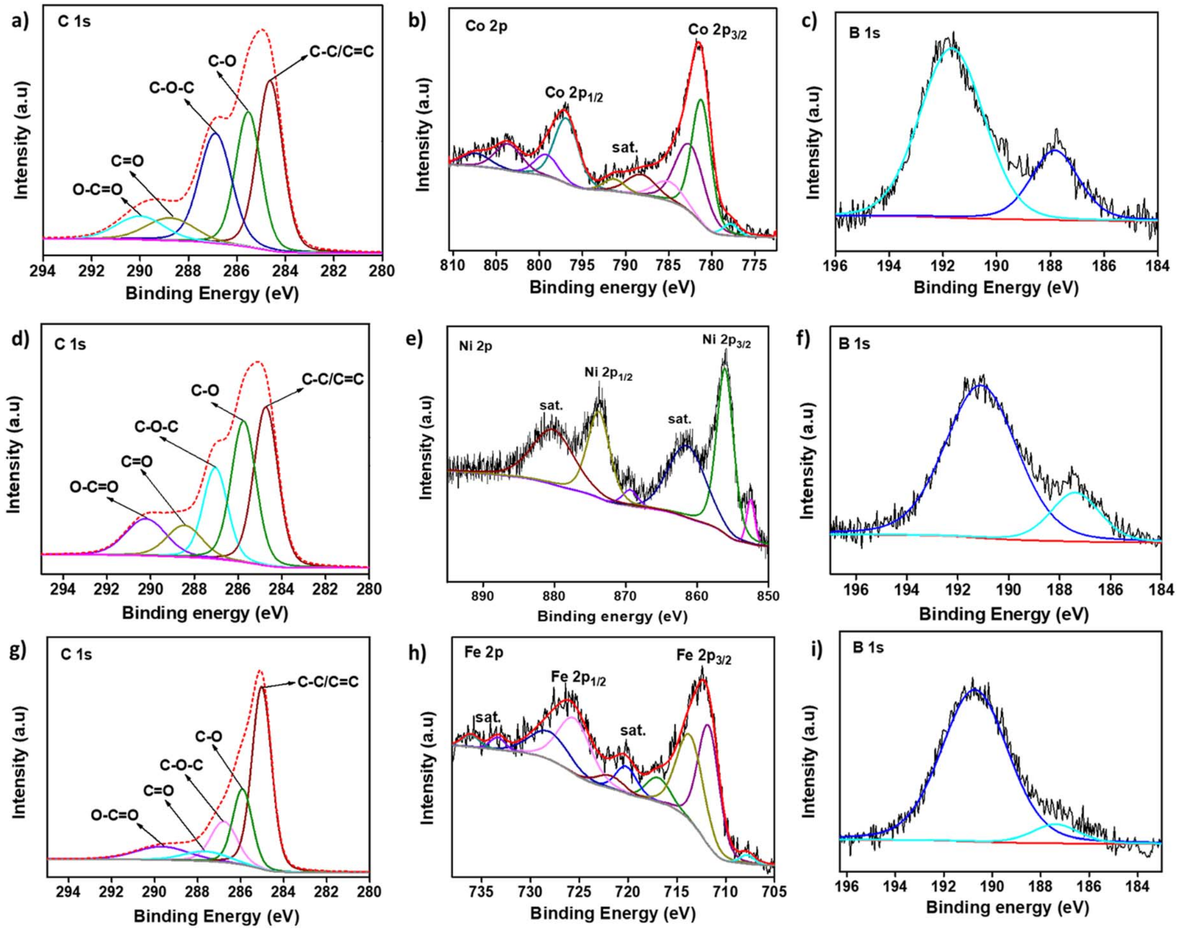

Fig. 4 XPS spectra of (a) C 1s, (b) Co 2p, and (c) B 1s for ON10/Co–B. XPS spectra of (d) C 1s, (e) Ni 2p and (f) B 1s for ON10/Ni–B. XPS spectra of (g) C 1s, (h) Fe 2p and (i) B 1s for ON10/Fe–B.

the most favourable electrocatalytic performance, which can be ascribed to the optimal combination of electrical conductivity provided by carbon and the active sites contributed by Co–B, thereby improving the catalytic efficiency.

The electrocatalytic activity of the prepared ON10 supported transition metal borides (ON10/Co–B, ON10/Ni–B and ON10/Fe–B) were compared and their respective LSV curves are shown in Fig. 5d. ON10/Co–B and ON10/Ni–B showed overpotentials of −122 mV and −190 mV, respectively, at 10 mA cm^{-2} current density. ON10/Fe–B showed poor activity towards the HER. Among the carbon-supported transition metal borides, ON10/Co–B showed the best electrocatalytic activity. The charge transfer resistance from EIS was found to be 3.31 Ω, 4.45 Ω, and 11.6 Ω for ON10/Co–B, ON10/Ni–B, and ON10/Fe–B, respectively (Fig. 5e). The high charge transfer resistance value for ON10/Fe–B explains the low HER activity of the catalyst. The Tafel slope values were found to be 136 mV/dec, 92 mV dec^{-1} and 146 mV dec^{-1} for ON10/Co–B, ON10/Ni–B, and ON10/Fe–B, respectively, indicating the Volmer-Heyrovsky mechanism, as shown in Fig. 5f. Typically, the enhanced electrocatalytic performance is correlated with a higher electrochemically active surface area (ECSA). ECSA serves as an indicator of the number of active sites available on the catalyst surface, and is directly proportional to the double-layer capacitance (C_{dl}) measured at the electrode–electrolyte interface.[45] The C_{dl} values obtained from CV scans (Fig. S7) show that ON10/Co–B has the highest ECSA of 19.8 mF cm^{-2} while ON10/Ni–B and ON10/Fe–B have ECSA values of 17.5 mF cm^{-2} and 5.3 mF cm^{-2}, respectively (Fig. 5g). The superior electrocatalytic activity of ON10/Co–B is corroborated by the highest ESCA and low R_{ct}. This highlights a large number of active catalytic sites, contributing to the enhanced electrocatalytic efficiency of ON10/Co–B. Additionally, the intrinsic catalytic activity was assessed by analyzing the LSV curves normalized to the double-layer capacitance. As shown in the ECSA-normalized plots (Fig. S8), ON10/Co–B consistently outperforms the other catalysts, demonstrating the highest intrinsic activity per active site. This enhanced ECSA is attributed to the abundant active sites generated by the uniform dispersion of Co–B particles on the ON10 support, while the mesoporous structure of ON10 facilitates effective electron transport at the electrode–electrolyte interface, thereby boosting the electrocatalytic performance of ON10/Co–B. Fig. 5h compares the electrocatalytic performance of ON10/Co–B with other carbon- and cobalt-based electrocatalysts. The results indicate that ON10/Co–B exhibits performance that is either better or on par with several benchmark electrocatalysts.

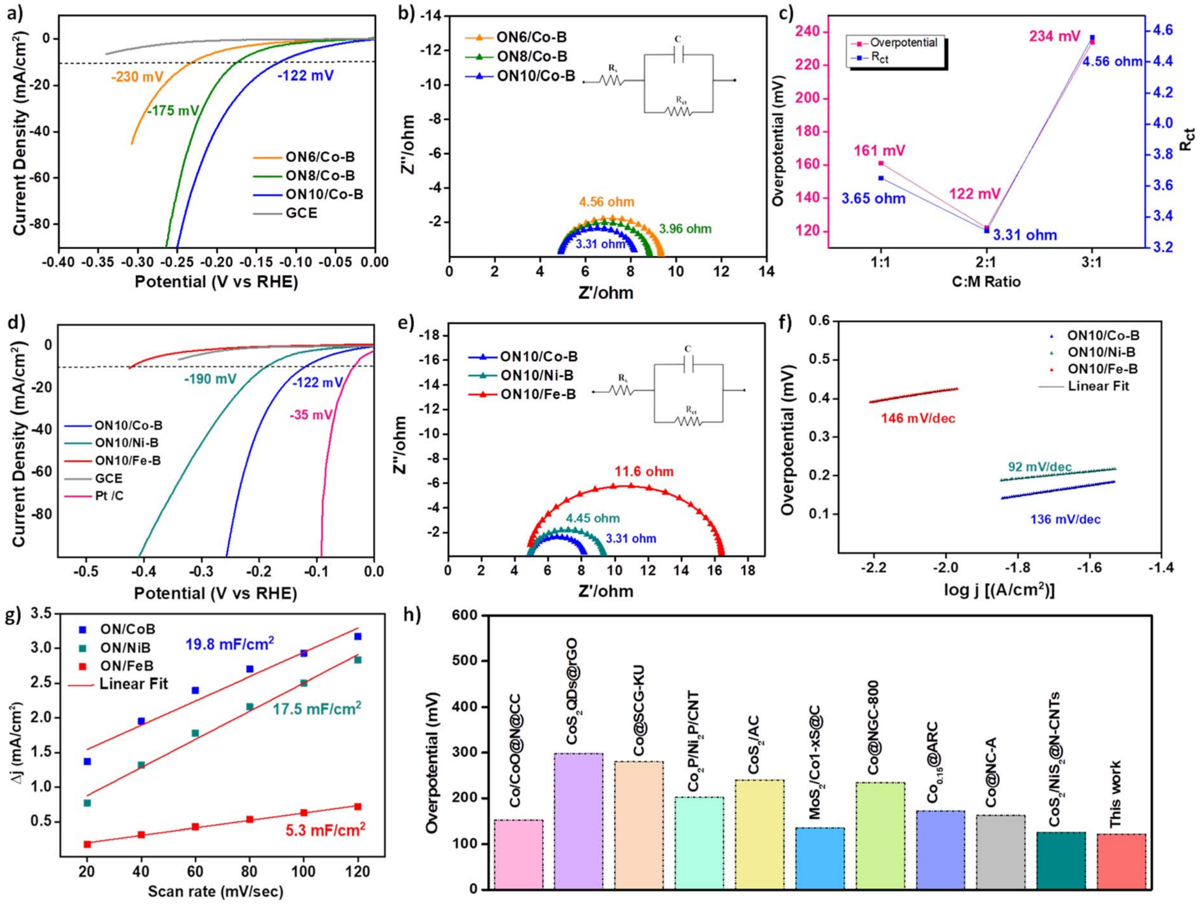

Fig. 5 (a) Linear polarization curves and (b) Nyquist plots of ON6/Co–B, ON8/Co–B, and ON10/Co–B for the HER in 1 M KOH; inset showing the fitted equivalent circuit. (c) Variation in R_{ct} and overpotential with variation in the C : M ratio in ON10/Co–B. (d) Linear polarization curves. (e) Nyquist plot; inset showing the fitted equivalent circuit. (f) Tafel plot. (g) Graph depicting the variation in cathodic and anodic current densities at different scan rates used to evaluate the C_{dl} values of ON10/Co–B, ON10/Ni–B, and ON10/Fe–B for the HER. (h) Comparative analysis of the overpotential value at 10 mA cm^{-2} of ON10/Co–B relative to carbon- and cobalt-based electrocatalysts reported in the literature for the HER.[35–44]

Post-reaction FESEM images (Fig. S9a) show that ON10/Co–B retains its morphology after the HER, demonstrating good structural stability, while the slight agglomeration observed probably results from the reaction conditions. The EDS analysis confirmed the presence of C, Co, B and O post HER (Fig. S9b).

The robustness of the electrocatalyst was evaluated by the stability and durability tests of the catalyst. Fig. 6a shows the LSV curves before and after 1000 cycles of the HER. ON10/Co–B showed a negligible change in overpotential for the HER even after 1000 cycles, indicating the efficiency of the synthesized

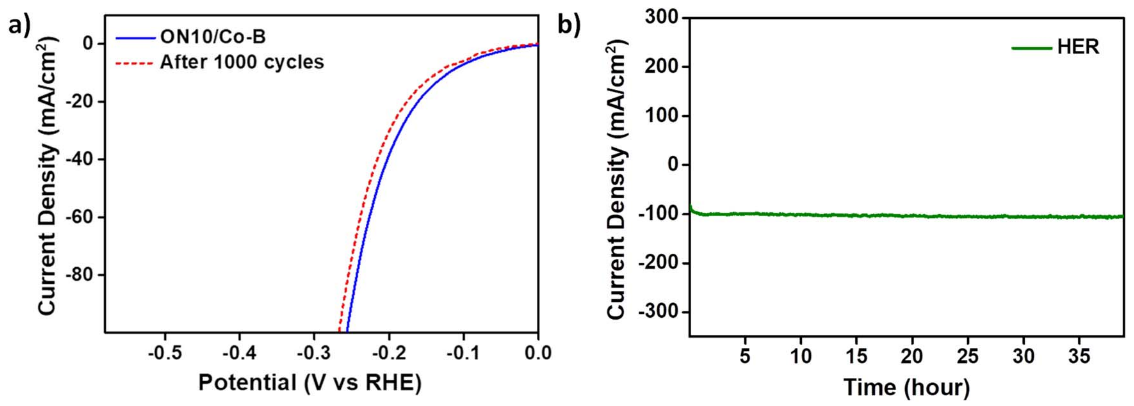

Fig. 6 (a) Linear polarization curves for the HER before and after 1000 cycles. (b) Chronoamperometric plot of ON10/Co–B for 40 h.

electrocatalyst. The stability of ON10/Co–B was examined by a chronoamperometric test. ON10/Co–B showed considerable stability towards the HER for 40 hours, as shown in Fig. 6b. The results confirm that the synthesized catalyst exhibits good stability and proves to be a promising material for the HER. Additionally, the Nyquist plot of ON10/Co–B obtained after the stability test of the HER shows only a slight change in R_{ct}, after the chronoamperometric analysis, which further supports the catalyst's durability (Fig. S10). Specifically, for the HER, the R_{ct} value increased marginally from 3.31 Ω to 3.8 Ω. These minimal changes indicate that the catalyst retains its conductivity and interfacial charge transfer capability even after extended electrochemical testing. Long-term stability is closely linked to the optimization of water-exposed catalytic interfaces. Controlled wettability, stable oxygen vacancy populations, and resistance to surface reconstruction help suppress catalyst dissolution and ensure sustained charge transfer. In the examined material, the amorphous-crystalline heterostructure provides a robust interface that maintains activity during extended electrolysis. Hence, these tests confirm that the synthesized catalyst exhibits good stability and shows capability as an effective candidate for the HER.

From the physicochemical and electrochemical studies discussed above, ON10/Co–B serves as an efficient electrocatalyst due to the combined effect of CNSs and Co–B. The enhanced electrical conductivity, disordered carbon that helps in enhancing the active sites for electrocatalytic reactions, amorphous nature of the catalyst, optimal C : M ratio, improved electron movement at the electrode/electrolyte interface due to the porous nature of the carbon, reverse electron transfer mechanism exhibited by Co–B, spherical morphology of the carbon support, and enhanced dispersion of Co–B nanoparticles on ON10 led to a large amount of active sites. ON10/Co–B was prepared through a two-step, activation-free process using a sustainable carbon source obtained from biowaste. This approach not only delivers an efficient and cost-effective electrocatalyst but also illustrates a "waste-to-wealth" concept by transforming biomass waste into a valuable electrocatalyst.

Conclusions

In summary, carbon nanospheres synthesized from onion peels were combined with transition metal borides by a chemical reduction method. Among the samples, ON10/Co–B showed the best electrocatalytic performance with an overpotential of −122 mV for the HER at a current density of 10 mA cm^{-2}. The catalyst maintained its activity over long-term stability tests, showing consistent performance during 40 hours of chronoamperometric operation and after 1000 continuous LSV cycles. The electrocatalytic performance of ON10/Co–B can be ascribed to its unique composition, uniform distribution of Co–B nanoparticles on the carbon matrix with an appropriate particle size of the carbon support, its mesoporous nature and high ECSA. This study introduces a facile and sustainable method for converting biomass into a catalyst support, providing insights into the design and development of electrocatalysts and their application in alkaline water splitting.

Author contributions

B. Sirichandana: conceptualization, methodology, analysis, investigation, writing – original draft preparation. R. Silviya: data curation, analysis, editing. Uraiwan Sirimahachai: visualization, investigation. Nainesh Patel: writing – reviewing and editing. Gurumurthy Hegde: supervision, writing – reviewing and editing.

Conflicts of interest

There are no conflicts to declare.

Data availability

No primary research results, software or code have been included and no new data were generated or analysed as part of this review.

Supplementary information is available. See DOI: **https://doi.org/10.1039/d5ra05923b**.

Acknowledgements

One of the authors B. Sirichandana (CHE-05/2024-25) acknowledges the assistance provided by KSTePS, DST, Govt. of Karnataka. N. Patel thanks the Department of Science and Technology (DST), Ministry of Science and Technology, India, for providing funds under the AHFC project (DST/TMD-EWO/AHFC-2021/100), Indo-Italian Project (INT/Italy/P-42/2022(ER)(G)) and FIST program (SR/FST/PS-I/2022/208). N. Patel would like to acknowledge the Board of Research in Nuclear Sciences, DAE, India, for funding the project (51/14/03/2023-BRNS/11376). The authors also thank Prof Arvind Jadhav, CNMS, Jain University, for his help in initial discussions.

References

1 H. Ozcan, R. S. El-Emam, S. Celik and B. A. Horri, *Clean. Chem. Eng.*, 2023, 100115.
2 X. Li, X. Hao, A. Abudula and G. Guan, *J. Mater. Chem. A*, 2016, **4**, 11973–12000.
3 H. Irshad, M. Zia, R. Al-Hajri, Z. A. K. Khattak, M. Al-Abri, N. Ahmad and H. A. Younus, *Int. J. Hydrogen Energy*, 2025, **137**, 1009–1041.
4 X. Yang, R. Guo, R. Cai, W. Shi, W. Liu, J. Guo and J. Xiao, *Dalton Trans.*, 2022, **51**, 4590–4607.
5 A. H. Al-Naggar, N. M. Shinde, J.-S. Kim and R. S. Mane, *Coord. Chem. Rev.*, 2023, **474**, 214864.
6 Y. Jiang and Y. Lu, *Nanoscale*, 2020, **12**, 9327–9351.
7 X. Cao, J. E. Medvedeva and M. Nath, *ACS Appl. Energy Mater.*, 2020, **3**, 3092–3103.
8 Y. Chen, Y. Fan, Z. Cui, H. Huang, D. Cai, J. Zhang, Y. Zhou, M. Xu and R. Tong, *Int. J. Hydrogen Energy*, 2023, **48**, 27992–28017.
9 J. Su, J. Zhou, L. Wang, C. Liu and Y. Chen, *Sci. Bull.*, 2017, **62**, 633–644.

10 J. Masa, P. Weide, D. Peeters, I. Sinev, W. Xia, Z. Sun, C. Somsen, M. Muhler and W. Schuhmann, *Adv. Energy Mater.*, 2016, **6**, 1502313.

11 S. Gupta, N. Patel, A. Miotello and D. C. Kothari, *J. Power Sources*, 2015, **279**, 620–625.

12 A. Chunduri, S. Gupta, O. Bapat, A. Bhide, R. Fernandes, M. K. Patel, V. Bambole, A. Miotello and N. Patel, *Appl. Catal., B*, 2019, **259**, 118051.

13 Q. Hu, G. Li, Z. Han, Z. Wang, X. Huang, H. Yang, Q. Zhang, J. Liu and C. He, *J. Mater. Chem. A*, 2019, **7**, 14380–14390.

14 W. Zhang, R. Xi, Y. Li, Y. Zhang, P. Wang and D. Hu, *Int. J. Hydrogen Energy*, 2022, **47**, 32436–32454.

15 J. Deng, M. Li and Y. Wang, *Green Chem.*, 2016, **18**, 4824–4854.

16 Z. Liu, Q. Ling, Y. Cai, L. Xu, J. Su, K. Yu, X. Wu, J. Xu, B. Hu and X. Wang, *Nanoscale Adv.*, 2022, **4**, 1246–1262.

17 S. Supriya, G. Sriram, Z. Ngaini, C. Kavitha, M. Kurkuri, I. P. De Padova and G. Hegde, *Waste Biomass Valorization*, 2020, **11**, 3821–3831.

18 A. Nieto-Márquez, R. Romero, A. Romero and J. L. Valverde, *J. Mater. Chem.*, 2011, **21**, 1664–1672.

19 J. P. Reddy and J.-W. Rhim, *J. Nat. Fibers*, 2018, **15**, 465–473.

20 H. Yang, R. Yan, H. Chen, C. Zheng, D. H. Lee and D. T. Liang, *Energy Fuels*, 2006, **20**, 388–393.

21 K. Bijapur, S. Mandal, P. G. Siddheshwar, S. Bose and G. Hegde, *Nanoscale*, 2025, **17**, 10239–10249.

22 V. C. Hoang, V. G. Gomes and K. N. Dinh, *Electrochim. Acta*, 2019, **314**, 49–60.

23 G. Soman, V. Molahalli, K. Sayeed, K. Pandey, B. B. Kulkarni and G. Hegde, *J. Energy Storage*, 2025, **111**, 115373.

24 V. S. Bhat, T. J. Jayeoye, T. Rujiralai, U. Sirimahachai, K. F. Chong and G. Hegde, *Front. Energy Res.*, 2021, **9**, 744133.

25 G. Fu, Q. Li, J. Ye, J. Han, J. Wang, L. Zhai and Y. Zhu, *J. Mater. Sci.: Mater. Electron.*, 2018, **29**, 7707–7717.

26 Y. Jiang, Y. Fang, C. Chen, P. Ni, B. Kong, Z. Song, Y. Lu and L. Niu, *Chemelectrochem*, 2019, **6**, 3684–3689.

27 S. Anantharaj and S. Noda, *Small*, 2020, **16**, e1905779.

28 B. Guan, L. Fan, X. Wu, P. Wang, Y. Qiu, M. Wang, Z. Guo, N. Zhang and K. Sun, *J. Mater. Chem. A*, 2018, **6**, 24045–24049.

29 V. Jose, J. M. V. Nsanzimana, H. Hu, J. Choi, X. Wang and J.-M. Lee, *Adv. Energy Mater.*, 2021, **11**, 2100157.

30 A. Shetty, B. G. Bag, U. Sirimahachai and G. Hegde, *Catal. Sci. Technol.*, 2025, **15**, 1525–1537.

31 R. Silviya, Y. Vernekar, A. Bhide, S. Gupta, N. Patel and R. Fernandes, *ChemCatChem*, 2023, **15**, e202300635.

32 X. Chen, Z. Yu, L. Wei, Z. Zhou, S. Zhai, J. Chen, Y. Wang, Q. Huang, H. E. Karahan, X. Liao and Y. Chen, *J. Mater. Chem. A*, 2019, **7**, 764–774.

33 T. Xie, G. Song, G. Wang, P. Feng, H. Xu, K. Lv and Y. Zhu, *J. Electron. Mater.*, 2022, **51**, 3705–3713.

34 B. Sirichandana, R. Silviya, S. V. Bhat, N. Patel and G. Hegde, *Nanoscale Adv.*, 2025, **7**, 4056–4066.

35 K. Dai, N. Zhang, L. Zhang, L. Yin, Y. Zhao and B. Zhang, *Chem. Eng. J.*, 2021, **414**, 128804.

36 J. Jiang, R. Sun, X. Huang, H. Cong, J. Tang, W. Xu, M. Li, Y. Chen, Y. Wang, S. Han and H. Lin, *Chem. Eng. J.*, 2022, **430**, 132634.

37 B. Sukhbaatar, S. Yoon and B. Yoo, *J. Mater. Sci.*, 2022, **57**, 18075–18088.

38 Z. Ding, H. Yu, X. Liu, N. He, X. Chen, H. Li, M. Wang, Y. Yamauchi, X. Xu, M. A. Amin, T. Lu and L. Pan, *J. Colloid Interface Sci.*, 2022, **616**, 210–220.

39 S. B. Devi and R. Navamathavan, *J. Electrochem. Soc.*, 2023, **170**, 026504.

40 M.-Y. Ma, H.-Z. Yu, L.-M. Deng, L.-Q. Wang, S.-Y. Liu, H. Pan, J.-W. Ren, M. Y. Maximov, F. Hu and S.-J. Peng, *Tungsten*, 2023, **5**, 589–597.

41 R. Kalusulingam, K. Ravi, S. Mathi, T. S. Mikhailova, K. Srinivasan, A. V. Biradar and T. N. Myasoedova, *Colloids Surf. A Physicochem. Eng. Asp.*, 2024, **692**, 133959.

42 Y. Zhou, Y. Luo, Q. Li, J. Liang, F. Liu, Y. Cai, L. Lin, Q. Wu and K. Li, *Energy Fuels*, 2024, **38**, 15560–15570.

43 W. Han, F. Zhang, Y. He, C. Yu, L. Lei and X. Zhang, *Electrochim. Acta*, 2024, **476**, 143735.

44 W. Xia, C. Li, L. Zhang, X. Yu, L. Zheng, R. Liu and A. Lv, *Colloids Surf. A Physicochem. Eng. Asp.*, 2025, **713**, 136547.

45 R. Fernandes, A. Chunduri, S. Gupta, R. Kadrekar, A. Arya, A. Miotello and N. Patel, *Electrochim. Acta*, 2020, **354**, 136738.